Comput Mech (2009) 43:277–295
DOI 10.1007/s00466-008-0305-z

ORIGINAL PAPER

Numerical investigation of crack growth in concrete subjected to compression by the generalized beam lattice model

J. X. Liu · Z. Y. Zhao · S. C. Deng · N. G. Liang

Received: 17 December 2007 / Accepted: 20 May 2008 / Published online: 18 June 2008

Abstract The beam lattice-type models, such as the Euler–Bernoulli (or Timoshenko) beam lattice and the generalized beam (GB) lattice, have been proved very effective in simulating failure processes in concrete and rock due to its simplicity and easy implementation. However, these existing lattice models only take into account tensile failures, so it may be not applicable to simulation of failure behaviors under compressive states. The main aim in this paper is to incorporate Mohr–Coulomb failure criterion, which is widely used in many kinds of materials, into the GB lattice procedure. The improved GB lattice procedure has the capability of modeling both element failures and contact/separation of cracked elements. The numerical examples show its effectiveness in simulating compressive failures. Furthermore, the influences of lateral confinement, friction angle, stiffness of loading platen, inclusion of aggregates on failure processes are respectively analyzed in detail.

Keywords GB lattice model · Compressive test · Mohr–Coulomb criterion · Fracture · Concrete · Lattice mode

J. X. Liu (✉) · Z. Y. Zhao
School of Civil and Environmental Engineering,
Nanyang Technological University, 639798 Singapore, Singapore
e-mail: taibaijinxing@gmail.com

S. C. Deng
Key laboratory of High Temperature Gas Dynamics (LHD),
Institute of Mechanics, Chinese Academy of Sciences,
100080 Beijing, China

N. G. Liang
State Key Laboratory of Nonlinear Mechanics (LNM),
Institute of Mechanics, Chinese Academy of Sciences,
100080 Beijing, China

1 Introduction

1.1 Short review of lattice-type fracture models

Fracture processes in heterogeneous materials such as rock and concrete are very difficult to interpret without appealing to their microstructures (see for instance [20,32]). As for concrete, the beam lattice model allows for a straightforward implementation of the heterogeneity of the three-phase system: aggregate, matrix and interface between them [21,25–28,34,35,40]. There are arguments on the inclusion of elemental bending deformations. For example, Cusatis et al. [9] pointed out that the bending of beams is not a characteristic of the physical phenomena in the microstructure, and calculated the shear strain assuming that influence zones of nodes are rigid. At the same time, however, they also considered the nodal rotations, and their proposed elements (called connecting struts in [9]) also behave somewhat like beam elements [3,22]. Chang et al. [5] have also shown the close relationship between a lattice of beams [17,34,35] and a network of particles [1,4,13,42]. Furthermore, beam elements have the following advantage: When elements are removed during simulation a substantial part of the lattice may be connected to the reminder of the lattice through a single element only. When either truss elements or springs (with free rotations at their ends) are used instead of beams, the computation becomes unstable [21,25,36]. This instability disappears naturally in beam lattices. The GB lattice model was recently developed by [26–28] and is also a kind of beam lattices. All investigations in this paper are based on the GB lattice model.

Another attractive feature of the beam lattice models lies in its ability to simulate different stress states on different orientations around a single node without any increase of computational effort. As shown in Fig. 1, node i has interactions

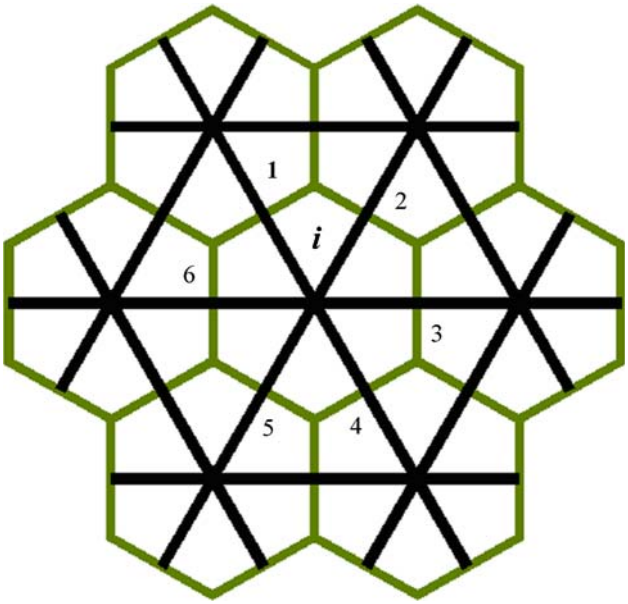

Fig. 1 The typical sketch-map of lattice-type beam models

with the six nodes around it, and the six interactions are represented by six GB elements numbered 1–6, respectively. Under the external actions, the six GB elements have independent deformations, indicating that node i is permitted to deform differently along directions of the six GB elements. This feature gives the GB lattice a great advantage over both the distinct element method (DEM), which takes nodes (particles) as rigid [8,31], and the discontinuous deformation analysis (DDA) theory, which assumes a constant strain state throughout every block [6,37,38]. Due to the same reason, beams of different orientations can be assigned different material properties in order to simulate behaviors of anisotropic materials. Additionally, the lattice-type beam models (not truss-lattices) are naturally capable of reproducing the size effect due to the change of the microstructure characteristic size [12,39]. Finally, Ostoja-Starzewski [29,30] gave a more systematic and detailed review on both basic theories and applications of lattice models.

The two-dimensional GB lattice model is employed in this paper. Of course, the 3D model is a more realistic approximation of materials because the micro structure in concrete is 3D in nature. However, the calibration of elemental parameters remains a crucial difficulty even though the difficulty in computational effort can be overcome with the rapid development of computer hardware. In fact, we are investigating the 3D modeling which will be a future topic.

There are mainly two methods to take the material heterogeneity into consideration in the lattice-type beam model, that is, *direct projection* [2,21,25,34], and *indirect statistical assignment of material properties* [40,43]. The former can obtain more realistic results than the latter, but leads to a substantial increase of the computational effort [2,40]. To solve the problem of computational effort, the generalized beam (GB) lattice model was developed by [26–28]. The key idea of GB lattice is the proposal of a kind of two-node and three-segment element. When the computational effort is not the choke point, GB lattice model can also simulate the geometry of aggregates more accurately than the classical beam lattice [28]. In this paper, in order to obtain more detailed crack growth, numerical simulations are mainly conducted based on the GB lattice model proposed in [28] where every big aggregate is simulated by dozens of nodes, and only one compressive example is done based on the lattice proposed in [26,27] where every aggregate is represented by only one node.

1.2 Extension of the GB lattice model to analyses of compressive failures

One of big challenges for lattice-type beam models is simulation of compressive failure processes. The most widely used field of this kind of models is in the concrete/rock fracture analyses. In practical engineering environments, these two kinds of materials mainly serve under compressive states. In the laboratory compressive tests, the vast majority of fractured elements consist of the compression-induced tensile cracks in the low loading stage, which are expected to be captured by the beam lattice models with maximum effective tensile stress/strain criterion [21,26,40]. As is generally known, however, the shearing deformation is dominant in compressive failures and the corresponding fracture mechanism is usually described as Mohr–Coulomb criterion, which takes the shear deformation into consideration as well as the normal deformation [3]. As a result, the existing beam lattice models can not accurately simulate compressive failures. This problem seriously shrinks their application range.

In this paper, we aim to extend the GB lattice model to the compressive failure analysis. The Mohr–Coulomb criterion is used as the strength criterion to judge successive failures of critical elements. Due to the relatively low tension strength, the tension-cut-off Mohr–Coulomb curve is adopted [3]. In compressive failures, the contact analysis between crack surfaces is crucial. In this paper, under the assumption of smooth-contact between contacting surfaces, there only exist normal interactions, therefore two contacting nodes (particles) can be represented by a link element without tension resistance. Of course, the smooth contact assumption may be too rough an approximation of reality, but interlocking of crack surfaces happens frequently due to the heterogeneous nature of concrete/rock in the meso-level. The interlocking mechanism plays a more dominant role than the friction in the sliding between crack surfaces, so the numerical procedure in this paper is still effective to simulate the essential features of compressive failures. It is

notable that the algorithm in this paper can be also used in the classical beam lattices.

The paper is structured as follows. The basic theory of the GB lattice model is recalled in Sect. 2. The Mohr–Coulomb criterion and the nonlinear algorithm are introduced in Sect. 3. In Sect. 4, several numerical examples are given to verify the effectiveness of the numerical procedure and to analyze influences of different factors on the fracture processes in concrete subjected to compression. The paper ends with conclusions in Sect. 5.

2 GB lattice model

In this model proposed by [26–28], a kind of two-node and three-phase elements has been developed. Every element is composed of three beams, which can be aggregate-phase, matrix-phase or interface-phase independently (Fig. 2). As a result, an aggregate can be simulated in principle by a single node in the GB lattice, instead of 10–100 nodes in other beam lattices [21,40]. Therefore the computational effort is reduced greatly.

In the three-fragment GB element, every fragment is regarded as a beam. These beams can be taken as Euler-Bernoulli beams, Timoshenko beams or beams proposed by [3]. No matter which beam theory is adopted, the beam stiffness matrices have the following common expression (Fig. 3):

$$\begin{Bmatrix} Q_1 \\ N_1 \\ M_1 \\ Q_2 \\ N_2 \\ M_2 \end{Bmatrix} = \underbrace{\begin{bmatrix} \mathrm{M}_{11} & 0 & -\mathrm{M}_{34} & -\mathrm{M}_{11} & 0 & -\mathrm{M}_{34} \\ & \mathrm{M}_{22} & 0 & 0 & -\mathrm{M}_{22} & 0 \\ & & \mathrm{M}_{33} & \mathrm{M}_{34} & 0 & \mathrm{M}_{36} \\ & & & \mathrm{M}_{11} & 0 & \mathrm{M}_{34} \\ & & \mathrm{SYM} & & \mathrm{M}_{22} & 0 \\ & & & & & \mathrm{M}_{33} \end{bmatrix}}_{M} \begin{Bmatrix} u_1 \\ v_1 \\ \varphi_1 \\ u_2 \\ v_2 \\ \varphi_2 \end{Bmatrix} \tag{1}$$

where, $\mathbf{F}_{12} = \{Q_1\ N_1 M_1 Q_2 N_2\ M_2\}^T$ and $\mathbf{u}_{12} = \{u_1\ v_1 \varphi_1\ u_2 v_2\ \varphi_2\}^T$ are the generalized force vector and the generalized displacement vector, respectively.

For the Euler–Bernoulli beam [12,29,30]:

$$\mathrm{M}_{11} = \frac{12E^{(b)}I}{h^3}, \quad \mathrm{M}_{34} = \frac{6E^{(b)}I}{h^2}, \quad \mathrm{M}_{22} = \frac{E^{(b)}A}{h},$$
$$\mathrm{M}_{33} = \frac{4E^{(b)}I}{h}, \quad \mathrm{M}_{36} = \frac{2E^{(b)}I}{h} \tag{2}$$

For the Timoshenko beam [19,44]:

$$\mathrm{M}_{11} = \frac{12E^{(b)}I}{(1+b)h^3}, \quad \mathrm{M}_{34} = \frac{6E^{(b)}I}{(1+b)h^2}, \quad \mathrm{M}_{22} = \frac{E^{(b)}A}{h},$$
$$\mathrm{M}_{33} = \frac{E^{(b)}I(4+b)}{h(1+b)}, \quad \mathrm{M}_{36} = \frac{E^{(b)}I(2-b)}{h(1+b)} \tag{3}$$

where, $E^{(b)}$ is the Young's Modulus; $t^{(b)}, h$ and l are respectively the thickness, the span and the height of the Timoshenko beam; $A = t^{(b)}l$ is the cross-section area; $I = t^{(b)}l^3/12$ is the moment of inertia; $b = aE^{(b)}l^2/G^{(b)}h^2$ is the dimensionless parameter in Timoshenko beam theory; $G^{(b)} = E^{(b)}/2(1+\nu^{(b)})$ is the modulus of rigidity, where $\nu^{(b)}$ is the Poisson's ratio.

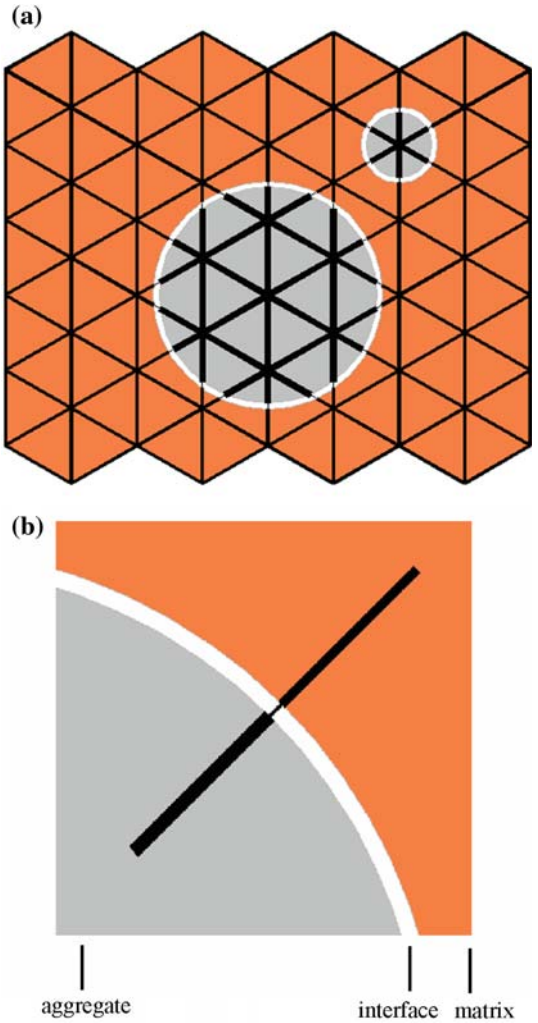

Fig. 2 A GB lattice: **a** projection of particle structure onto the lattice; **b** sketch-map of composition of an aggregate-interface-matrix element

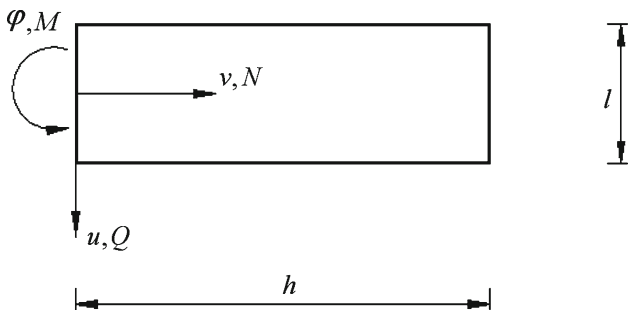

Fig. 3 Kinematics and statics of a beam

For the beam studied in [3]:

$$\mathrm{M}_{11}=\frac{G^{(b)}A}{h},\quad \mathrm{M}_{34}=\frac{G^{(b)}A}{2},\quad \mathrm{M}_{22}=\frac{E^{(b)\prime}A}{h},$$
$$\mathrm{M}_{33}=\frac{G^{(b)}Ah}{4}+\frac{E^{(b)\prime}I}{h},\quad \mathrm{M}_{36}=\frac{G^{(b)}Ah}{4}-\frac{E^{(b)\prime}I}{h} \tag{4}$$

where, $E^{(b)\prime}=E^{(b)}/[1-(\nu^{(b)})^2]$.

The relationship between the lattice and its continuum equivalent is obtained based on the equivalence of strain energy stored in a unit cell of a lattice with its continuum counterpart. The calibration results for a triangular GB lattice are listed as follows.

For the Euler–Bernoulli beam [29]:

$$E^{(b)}=\frac{E}{\sqrt{3}}\left(\frac{l}{h}\right)^{-1}\frac{t}{t^{(b)}}\frac{12+\left(\frac{l}{h}\right)^2}{4+\left(\frac{l}{h}\right)^2},\quad \nu=\frac{4-\left(\frac{l}{h}\right)^2}{12+\left(\frac{l}{h}\right)^2} \tag{5}$$

Note that the Poisson's ratio for Euler-Bernoulli beams is always zero.

For the Timoshenko beam [26]:

$$E^{(b)}=\frac{2}{\sqrt{3}}\left(\frac{l}{h}\right)^{-1}\frac{t}{t^{(b)}}\frac{E}{1-\nu},$$
$$\nu^{(b)}=\frac{5(1+\nu)}{11(1-3\nu)}-\frac{20}{11}\left(\frac{l}{h}\right)^{-2}-\frac{12}{11} \tag{6}$$

For the beam studied in [3]:

$$E^{(b)}=E,\quad \nu^{(b)}=\nu \tag{7}$$

The stiffness matrix of a GB element is expressed as functions of material and geometry parameters of its three beams. Take the element shown in Fig. 4 as an example, let $\mathbf{R}$ be the matrix relating the displacement vector $\mathbf{u}_{ij}=\{u_i\ v_i\ \varphi_i\ u_j\ v_j\ \varphi_j\}^T$ and $\mathbf{u}_{IJ}=\{u_I\ v_I\ \varphi_I\ u_J\ v_J\ \varphi_J\}^T$:

$$\mathbf{u}_{IJ}=\mathbf{R}\mathbf{u}_{ij} \tag{8}$$

Then the stiffness matrix of the GB element $\mathbf{K}$ can be expressed in the form

$$\mathbf{K}=\begin{bmatrix}\mathbf{M_I^a}+\mathbf{M_{II}^a}\mathbf{R_I} & \mathbf{M_{II}^a}\mathbf{R_{II}}\\ \mathbf{SYM} & (\mathbf{M_{II}^m})^{\mathbf{T}}\mathbf{R_{III}}+\mathbf{M_{III}^m}\end{bmatrix} \tag{9}$$

where, the superscript of $\mathbf{M}$ declares the material property; In other words,$\mathbf{M^m}$, $\mathbf{M^a}$ and $\mathbf{M^i}$ are respectively the stiffness matrix of matrix, aggregate and interface beams. $\mathbf{M_I^a}$, $\mathbf{M_{II}^a}$ and $\mathbf{M_{III}^a}$ denote the top-left, top-right and bottom-right 3×3 sub-matrix of $\mathbf{M^a}$, respectively, and the same notation rule

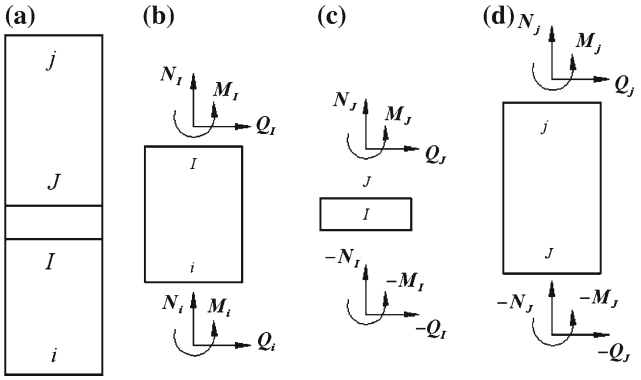

Fig. 4 A GB element composed of an aggregate beam, an interface beam and a matrix beam: **a** the GB element; **b** the aggregate beam; **c** the interface beam; **d** the matrix beam

is also used to $\mathbf{M^i}$ and $\mathbf{M^m}$.$\mathbf{R_I}$, $\mathbf{R_{II}}$and $\mathbf{R_{III}}$, respectively, denote the top-left, top-right, bottom-right 3×3 sub-matrix of $\mathbf{R}$.

It can be proved that the matrix $\mathbf{K}$ generally has the following distribution of non-zero elements:

$$\mathbf{K}=\begin{bmatrix}\mathrm{K}_{11} & 0 & -\mathrm{K}_{34} & -\mathrm{K}_{11} & 0 & -\mathrm{K}_{46}\\ & \mathrm{K}_{22} & 0 & 0 & -\mathrm{K}_{22} & 0\\ & & \mathrm{K}_{33} & \mathrm{K}_{34} & 0 & \mathrm{K}_{36}\\ & & & \mathrm{K}_{11} & 0 & \mathrm{K}_{46}\\ & & \mathrm{SYM} & & \mathrm{K}_{22} & 0\\ & & & & & \mathrm{K}_{66}\end{bmatrix} \tag{10}$$

It can be found that $\mathbf{K}$ in Eq. (10) has more independent elements than $\mathbf{M}$ in Eq. (1). For the sake of convenience, the following matrix $\mathbf{K}_\mathrm{N}$ is defined as

$$\mathbf{K}_N=\begin{bmatrix}0 & 0 & 0 & 0 & 0 & 0\\ & \mathrm{K}_{22} & 0 & 0 & -\mathrm{K}_{22} & 0\\ & & 0 & 0 & 0 & 0\\ & & & 0 & 0 & 0\\ & \mathbf{SYM} & & & \mathrm{K}_{22} & 0\\ & & & & & 0\end{bmatrix} \tag{11}$$

If the computational effort is the main choke point in the simulation, it is suggested to use the GB lattice in which every aggregate is modeled by a single node [26,27]. Otherwise, if the size of the simulated specimen is not very large and the main aim is to observe the failure process in more details, another kind of GB lattice is preferred, in which a single aggregate covers dozens of nodes [28]. The simulations in this paper are mainly based on the latter. Furthermore, every GB element is composed of three beams of the same span and the same depth, which are all described by the Timoshenko beam theory.

3 Mohr–Coulomb criterion and event-driven algorithm

3.1 Mohr–Coulomb criterion

Mohr–Coulomb theory is a mathematical model describing the response of materials such as rock, rubble piles or concrete to shear stress as well as normal stress. Most of the classical engineering materials somehow follow this rule in at least a portion of their shear failure envelope. The criterion can be expressed in the form

$$|\tau| < c - \sigma \tan\phi \tag{12}$$

where, c is the cohesive strength and ϕ is the friction angle; τ and σ are the shear stress and the normal stress, respectively.

Because materials such as concrete/rock have a very low tensile strength f_t as compared with their compressive strength and shear strength, the Mohr–Coulomb strength surface with tension cut-off [3] is adopted here (Fig. 5). Concrete's compressive strength f_c is generally 10–20 times the value of its tensile strength, so $f_c = 12 f_t$ is used in this paper. Furthermore, the failure surface in Fig. 5 can be expressed by the following three inequations:

$$\sigma < f_t \tag{13a}$$

$$|\tau| < c - \sigma \tan\phi \tag{13b}$$

$$\sigma > -f_c \tag{13c}$$

Then the implementation of the Mohr–Coulomb criterion shown in Fig. 5 is introduced. It is notable that we find out the critical element by checking the stresses in beams of GB

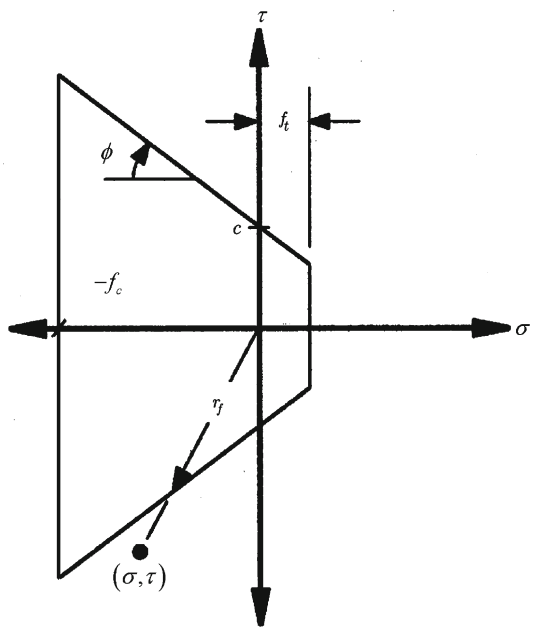

Fig. 5 Mohr–Coulomb strength surface with tension cut-off

elements. The normal stress can be expressed in the form [40]

$$\sigma = \frac{N}{A} + \alpha \frac{(|M_i|, |M_j|)_{\max}}{W} \tag{14}$$

where, N is the normal force in the considered beam, M_i and M_j are the bending moments at the nodes i and j of the beam, and $W = t^{(b)} l^2/6$ is the section modulus. The coefficient α regulates what part of the bending moment is considered. Lilliu and van Mier [25] have shown that simulation results are also satisfactory in the case of $\alpha = 0$ though α is usually set to 0.005 [21,26,40]. Therefore, α is also set to zero in this paper. Another advantage of α being zero lies in that three beams in every GB element have the uniform normal stress because both N and A are uniform throughout every GB element.

From Eq. (1), the shear force can be expressed in the form

$$Q_1 = -Q_2 = \mathrm{M}_{11}(u_1 - u_2) - \mathrm{M}_{34}(\varphi_1 + \varphi_2) \tag{15}$$

In consideration of the equilibrium conditions at I and J (Fig. 4), it can be found that the shear force is also uniform throughout the GB element. Therefore, the shear stress can be calculated as

$$|\tau| = \frac{|Q_1|}{A} = \frac{1}{A} |\mathrm{M}_{11}(u_1 - u_2) - \mathrm{M}_{34}(\varphi_1 + \varphi_2)| \tag{16}$$

Actually, in order to judge if a GB element becomes critical, it is not necessary to check all its three beams. Only its middle beam needs to be checked instead. The reasons are as follows:

- Both σ and τ are uniform in every GB element, which has been discussed above.
- In all GB elements, the strength of the middle beam is equal to or less than the strength of the other two beams. In three-phase materials, there are four kinds of GB elements: matrix–matrix–matrix, aggregate–aggregate–aggregate, matrix–interface–aggregate, and aggregate–interface–aggregate. For the first two kinds, three beams have the same strength. For the last two kinds, the middle beam is the weakest among three beams because the interfacial phase is the weakest phase among the three-phase system.

As a result, the efficiency of the numerical procedure is improved. Furthermore, it makes the following assumption reasonable: when some GB element becomes critical, it cracks into two fragments of the same span, that is, $L/2$, where L is the length of the GB element. Therefore, if all six GB elements starting from node i have failed, the isolated material domain around node i, called influence zone of node i has the geometry shown as Fig. 6a. The GB lattice can be also taken as a network by gluing a large amount of this kind of

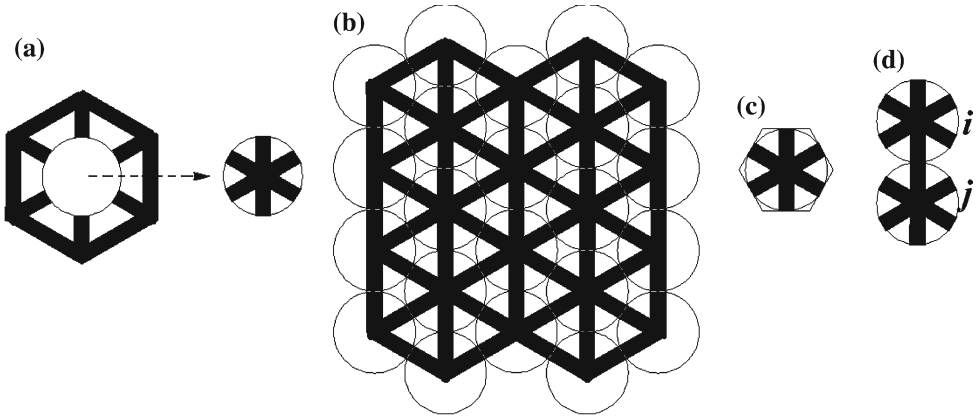

Fig. 6 A GB lattice with circular nodal influence zones: **a** a single nodal influence zone isolated be surrounding failures; **b** potential failure positions of the lattice; **c** comparison of circular and hexagon influence zones; **d** sketch-map of contact

material domains, shown as Fig. 6b, where the short line-segment crossing the middle of every GB element indicates the potential crack path.

Then an important approximation is made: the material domain around every node is circular and its diameter is L, which is the same as the bonded-particle model (BPM) [30]. The advantages of the GB lattice over the BPM will be discussed later. When calibrating the GB lattice [26], it is assumed that the influence zone (unit cell) is hexagonal, which is $\pi \Big/ 2\sqrt{3}$ times the area of the circle (Fig. 6c). This difference can be avoided easily when using the equivalence of strain energy between the GB lattice and its continuum counterpart. But this difference is neglected in this paper. On one hand, it does not influence the results seriously. On the other hand, even though the model is a very rough approximation of reality, this appears throughout all kinds of lattice-type approaches [25].

The adoption of circular influence zones (unit cells) brings the following two advantages at least:

- The contact detection becomes very simple. To judge if contact happens in a cracked element, we only need to compare the initial length of the element with the current distance between its two nodes. Although only cases of small displacements are studied here, the circular-influence-zone assumption can simplify the contact/separation detection when large displacements are permitted.
- The direct calculation of the stiffness matrix of recurred elements, that is, contact elements, becomes possible. If the crack path in an element is arbitrary, the corresponding contact stiffness can not be calculated directly in principle without any assumption. There are mainly two kinds of assumptions: one takes the influence zones as rigid bodies [8,31], while the other assumes that the stress field throughout every special influence zone is uniform [16,37]. As shown in Fig. 6d, when the cracked element ij contacts, the stiffness matrix of the contact element can be calculated directly because the properties of the two "half GB elements" are known. In this paper, we only study the simplest case—smooth contact. Therefore, the contact element can only bear compressive actions along the direction of element ij, and the stiffness matrix can be expressed in the form

$$\mathbf{K}_{\text{contact}} = (1 - D)\,\mathbf{K}_{\text{N}} \tag{17}$$

where, D is the damage factor due to the deformation history. Of course, the concept of the damage factor here is extremely rough as compared with the one in the classical damage mechanics which increases gradually with external loads [24]. However, D in Eq. (17) also indicates the degradation of material properties, so basically has the same physical meaning of the classical damage factor [23].

In this paper, it is assumed that the failure modes violating different inequations in Eqs. (13) may generally produce different damage factors. In the following of this section, the nonlinear algorithm is introduced for that general case.

3.2 Event-driven algorithm

Fracture under compression is simulated by successive occurrences of "events", which may be failure of critical intact or partly failed elements, or contact/separation of former cracked elements. Then, the essential of numerical simulation is to detect new event(s) correctly. The event-driven method (see for instance [7]), also called the event-by-event method [3,33] is adopted here. The value of load increment in every step depends on the appearance of new critical element(s). After a load increment is applied, the normal stress σ and the shear stress τ acting in each beam are compared with the fracture surface, the criterion for fracture is

$$R = \frac{r}{r_f} > 1 \tag{18}$$

where $r = \left(\sigma^2 + \tau^2\right)^{0.5}$ and r_f is as defined in Fig. 5. Analogously, the criterion for separation/contact of cracked elements is

$$R = \frac{\sqrt{(\Delta u)^2 + (L + \Delta v)^2}}{L} > 1 \quad \text{(contact} \rightarrow \text{separation)} \tag{19}$$

$$R = \frac{L}{\sqrt{(\Delta u)^2 + (L + \Delta v)^2}} > 1 \quad \text{(separation} \rightarrow \text{contact)} \tag{20}$$

where, $\Delta u = u_j - u_i$ and $\Delta v = v_j - v_i$ are relative displacements between nodes i and j in element ij (Fig. 6).

Only one event is permitted per computational cycle. If several elements have $R > 1$, the element with the highest $R > 1$ undergoes new event. As for the critical element, the update of stiffness matrix and the release of internal forces are introduced as follows:

(1) If Eq. (13a) is violated, $\{Q_i \;\; N_i \;\; M_i \;\; Q_j \;\; N_j \;\; M_j\}^T$ is released, and the element stiffness matrix $\mathbf{K}$ is set to zero. It is notable that this element is definitely under tensile state in the current step. However, this element is possible to recur due to contact in the following steps. Once contact happens, the recurred stiffness matrix is

$$\overset{\mathrm{T}}{\mathbf{K}} = (1 - \overset{\mathrm{T}}{D})\mathbf{K}_{\mathrm{N}} \tag{21}$$

where, the superscript "T" in $\overset{\mathrm{T}}{\mathbf{K}}$ and $\overset{\mathrm{T}}{D}$ represents "Tension". Thus, $\overset{\mathrm{T}}{D}$ denotes the damage factor due to the failure by violating Eq. (13a), that is, maximum tensile stress criterion. $\mathbf{K}_{\mathrm{N}}$ has been defined in Eq. (11).

(2) If Eq. (13b) is violated, there are two possible cases. In one case, the normal stress σ acting in the critical element is positive, that is, tensile stress, so the element is not possible to become contact at the very beginning of stress redistribution. As a result, $\{Q_i \;\; N_i \;\; M_i \;\; Q_j \;\; N_j \;\; M_j\}^T$ is released, and the element stiffness matrix $\mathbf{K}$ is set to zero. In the other case, σ is negative, that is, compressive stress, so the critical element becomes contacting once violation happens. Then, $\{Q_i \;\; \overset{\mathrm{MC}}{D} N_i \; M_i \; Q_j \;\; \overset{\mathrm{MC}}{D} N_j \;\; M_j\}^T$ is released, and the stiffness matrix is updated as

$$\overset{\mathrm{MC}}{\mathbf{K}} = (1 - \overset{\mathrm{MC}}{D})\mathbf{K}_{\mathrm{N}} \tag{22}$$

where, the superscript "MC" stands for "Mohr–Coulomb". $\overset{\mathrm{MC}}{D}$ denotes the damage factor due to the failure under the actions of both the shear stress and the normal stress, defined as Mohr–Coulomb criterion in Eq. (13b).

(3) Three kinds of elements are possible to violate Eq. (13c): intact elements, elements damaged by violating Eq. (13a) previously, and elements damaged by violating Eq. (13b) previously. As for intact elements, $\{Q_i \;\; \overset{\mathrm{C}}{D} N_i M_i \; Q_j \;\; \overset{\mathrm{C}}{D} N_j \;\; M_j\}^T$ is released, and the stiffness matrix is updated as

$$\overset{\mathrm{C}}{\mathbf{K}} = (1 - \overset{\mathrm{C}}{D})\mathbf{K}_{\mathrm{N}} \tag{23}$$

where, the superscript "C" represents "Compression". As for the second kind of elements, $\{Q_i \; (\overset{\mathrm{C}}{D} - \overset{\mathrm{T}}{D})N_i / (1 - \overset{\mathrm{T}}{D})M_i \; Q_j (\overset{\mathrm{C}}{D} - \overset{\mathrm{T}}{D})N_j / (1 - \overset{\mathrm{T}}{D}) \;\; M_j\}^T$ is released, and the stiffness matrix is set to $\overset{\mathrm{C}}{\mathbf{K}}$. As for the third kind of elements, $\{Q_i \; (\overset{\mathrm{C}}{D} - \overset{\mathrm{MC}}{D})N_i / (1 - \overset{\mathrm{MC}}{D})M_i \, Q_j (\overset{\mathrm{C}}{D} - \overset{\mathrm{MC}}{D})N_j / (1 - \overset{\mathrm{MC}}{D}) \; M_j\}^T$ is released, and the stiffness matrix is also set to $\overset{\mathrm{C}}{\mathbf{K}}$.

It can be found that the above numerical algorithm is much more complex than that for simulations of tensile failures [21,26,40], due to the inclusion of separation/contact phenomena.

4 Numerical examples and discussions

The compressive/tensile tests are performed on a GB lattice with a rectangular geometry of $117/10$ by $49\sqrt{3}/5$ cm. The employed lattice is triangular and has a total of 22,990 GB elements and 7,781 nodes. All elements are $\sqrt{3}/10$ cm long. The depth-to-span ratio is set to 1.0 for all beams. The load is applied to the lattice by setting a uniform displacement at the upper edge.

Seven examples called case 1–7 respectively are simulated.

The first example, case 1, has the following settings:

- The micro elastic and strength properties are shown as Table 1.
- The loading platens, that is, the upper edge and the bottom edge, have matrix-phase's elastic properties, and are 100 times of the strength of matrix-phase. All vertical translation degrees of freedom are fixed along the bottom edge, while a uniform compression is applied to the upper edge through a controlled displacement. The sketch of the numerical experiment is shown in Fig. 7.
- The left and right edges have free boundary conditions.
- A particle overlay including 286 aggregates of different sizes is employed.

Table 1 The micro elastic and strength properties of phases

	E (Mpa)	f_t (Mpa)	f_c (Mpa)	c (Mpa)	ϕ(°)	D
Aggregate	70,000	10.0	120.0	15.0	45	0.9
Interface	25,000	1.25	15.0	1.875	45	0.9
Matrix	25,000	5.0	60.0	7.5	45	0.9

In the table, $D = \overset{\mathrm{T}}{D} = \overset{\mathrm{MC}}{D} = \overset{\mathrm{C}}{D}$.

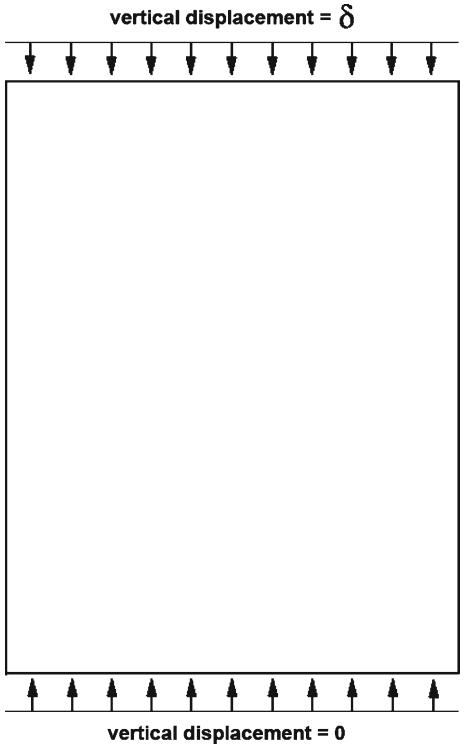

Fig. 7 Sketch of the numerical experiments

Case 2 is the same as case 1 except that a uniform tension instead of compression is applied to the upper edge.

Case 3 is the same as case 1 except that the horizontal translation degrees of freedom are fixed along both the left and right edges.

Case 4 is the same as case 1 except that the friction angle ϕ is 30° instead of 45°.

Case 5 has much stiffer upper and bottom loading platens, which are 5 times of the elastic modulus of loading platens in case 1.

Case 6 is the same as case 1 except that 3,000 aggregates with radii smaller than the element length L is projected to the lattice.

Case 7 is the same as case 1 except that no aggregate is projected on to the lattice. As a result, the lattice is purely matrix-phase.

4.1 Results

Figures 8, 9, 10, 11, 12, 13 and 14 show curves of reaction forces versus controlled displacements, curves of cumulative numbers of cracked elements versus controlled displacements, distributions of cracked elements and crack patterns for the seven cases, respectively. Figures of distributions of cracked elements and corresponding crack patterns may seem repetitious, but they are provided here for the reason: distributions of cracked elements show a more clear picture of both micro and macro cracks, while the crack patterns provide the relative relationships between cracks and material structures of the three-phase system. Figure 15 shows curves of cumulative numbers of cracked aggregate elements versus controlled displacements.

4.2 Fracture analyses

Case 1: Analyses of a typical compressive test

As observed from Fig. 8a, the fracture process can be separated by the peak load level "a" into two main branches, that is, pre- and post-peak branches. In the pre-peak stage, the reaction force P increases approximately linearly with controlled displacement δ, except a strong nonlinearity just before the peak point a. Many elements have failed at level a, and the vast majority of cracked elements consist of elements due to compression-induced tensile cracking (Fig. 8b, c). It is shown in Fig. 8d that cracked elements mainly concentrate in the interfacial zones between aggregates and surrounding matrix-phase, and form many local cracks parallel to the loading direction. This kind of fracture mechanism has also been observed by other investigators [14,31]. It can be imagined easily that local cracks parallel to the loading direction will not lead to obvious decrease of the specimen's capability of standing against deformation along the loading direction. This is the reason that P increases approximately linearly with δ during the pre-peak branch.

A steep drop of load, that is, from point a to point b, follows directly after the peak a (Fig. 8a). The steep drop is associated to the sharp increase of number of cracked elements (Fig. 8b). From Fig. 8e and f, the most remarkable phenomenon is the formation of a macroscopic crack band, which is roughly at the middle and near the right edge of the specimen. In this macro crack band, many matrix elements parallel to the loading direction have failed, leading to the steep drop of specimen's carrying capacity, that is, the a→b steep drop.

During b–c stage, P changes very irregularly with δ, but does not decrease (Fig. 8a). The number of cracked interface elements increases from 1,559 at level b to 3,187 at level c, while the number of cracked matrix elements increases from 340 at level b to 2,115 at level c (Fig. 8b). Therefore, most of failure events happen and macroscopic cracks form, grow and connect each other in this stage. Meanwhile, however, newly cracked elements parallel to the controlled displacement become contact elements, so still remain their normal stiffness. Observing Fig. 8g and h, we find the following toughening mechanism: extension of macroscopic crack bands is frequently deflected by aggregates, and forms the crack path in a zigzag shape, which leads to crack surfaces' interlocking and hampers the crack extension temporarily or changes the extension direction. Both contact phenomena and various toughening mechanisms hamper the decrease of reaction force P during the b–c stage.

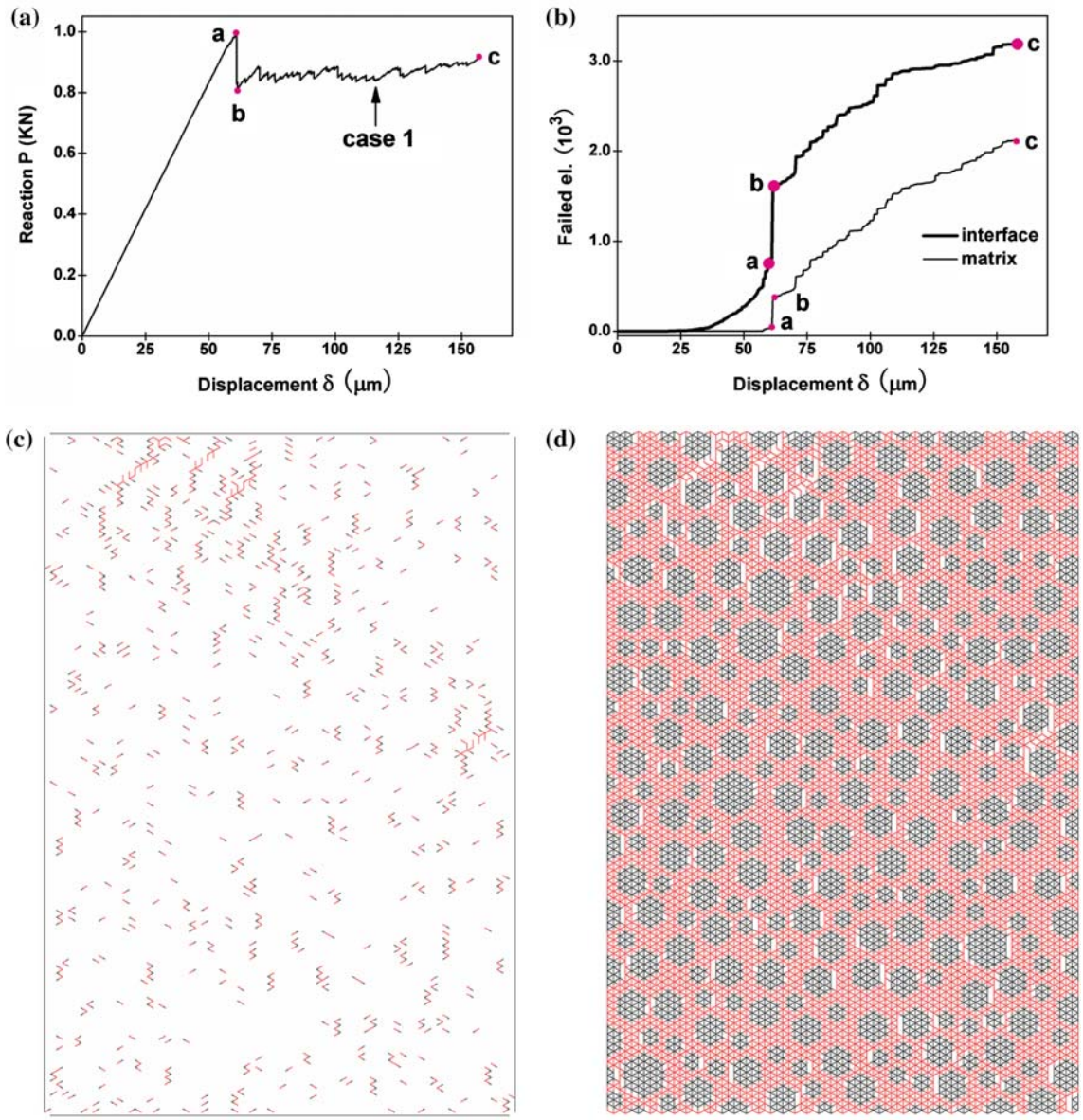

Fig. 8 In case 1, **a** the P-δ curve; **b** the cumulative number of cracked elements versus displacement; and distributions of cracked elements and crack patterns at three load levels: **c** and **d** for point a; **e** and **f** for point b; **g** and **h** for point c

Additionally, aggregate elements fail during the fracture process, which is reasonable at least for the parameter values used here (Table 1). This feature is different from tensile experiments based on lattice models where the fracture of aggregate elements is questionable. This can be explained as follows. In the three-phase system, the aggregate element has a tensile strength smaller than compressive strengths of the interface element and the matrix element even though the aggregate fraction is the strongest component of such a system. Figure 15 shows the cumulative number of failed aggregate elements versus displacement for different cases.

Case 2: Comparison of compressive test and tensile test

Detailed analyses of uniaxial tensile tests have been conducted by [26–28]. Here, the discussion will focus on the difference between case 2 and case 1.

After the steep drop a–b directly following the peak level a, the reaction force P becomes 18.7% of the peak load (Fig. 9a), much smaller than 83.5% in case 1. The explanation is as follows: macroscopic cracks nearly run through the specimen and separate the specimen into two parts (Fig. 9d), while the specimen is far from being separated by macroscopic cracks in case 1 (Fig. 8e, f). Furthermore, elements along the macroscopic crack fail due to tension in case 2. While elements along the macroscopic crack mainly fail due to compression or combined action of compression and shear, so these

Fig. 8 continued

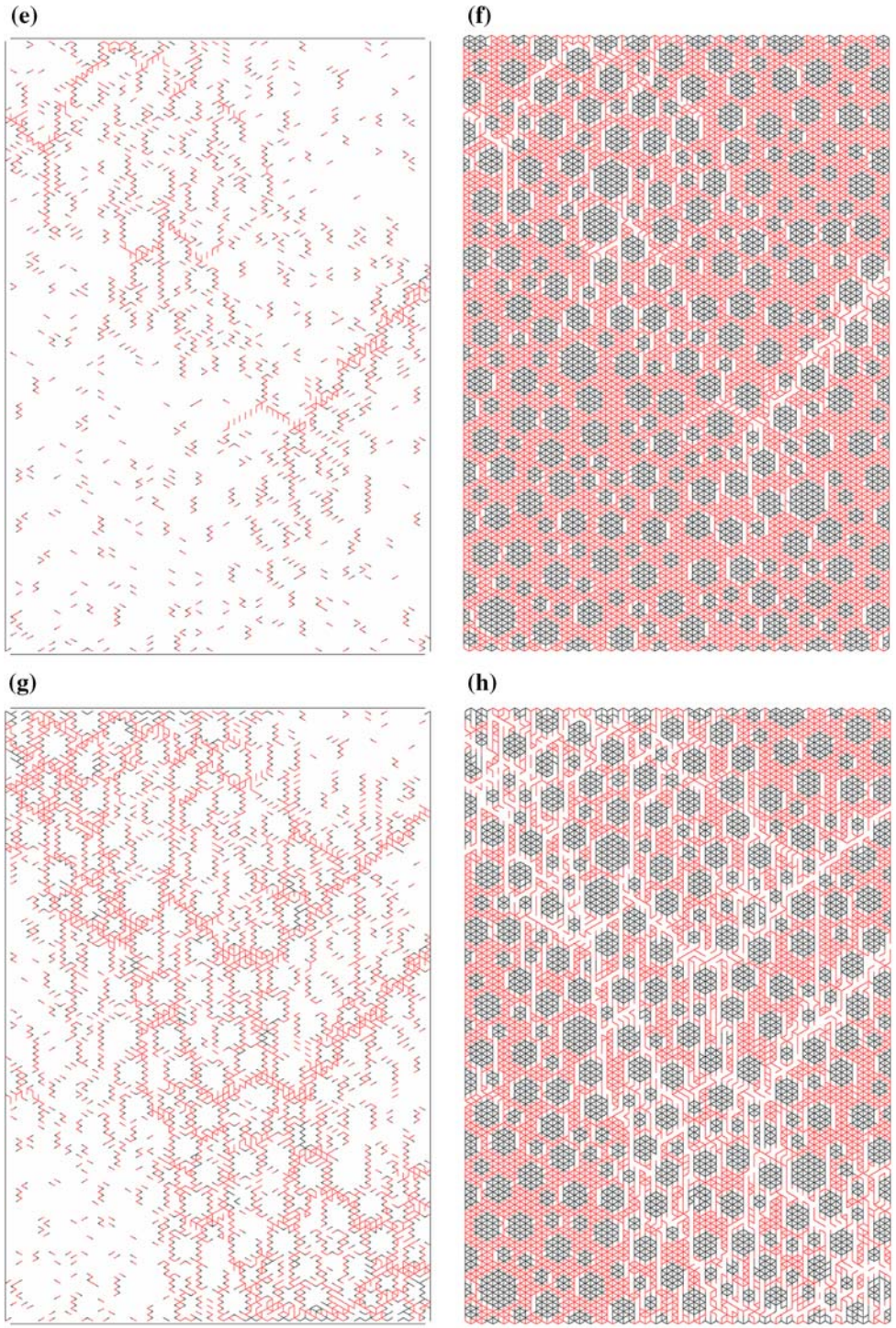

elements become contact elements and this contact mechanism is a kind of toughening mechanisms as stated in analyses of case 1.

The peak-load ratio of case 2 to case 1 is 1:13.8 (Fig. 9a), and not equal to $f_t / f_c = 1 : 12$ for three material-phases (Table 1). Is it questionable? The answer is NO for the following three reasons:

(1) The macroscopic behavior depends on both the micro material properties and the microstructure. The heterogeneous material structure has an important influence on macroscopic properties [26,32].

(2) The carrying capacity of the specimen depends on the strength distribution along potential macroscopic cracks [20,40]. Case 2 has a macroscopic crack path completely different from that of case 1.

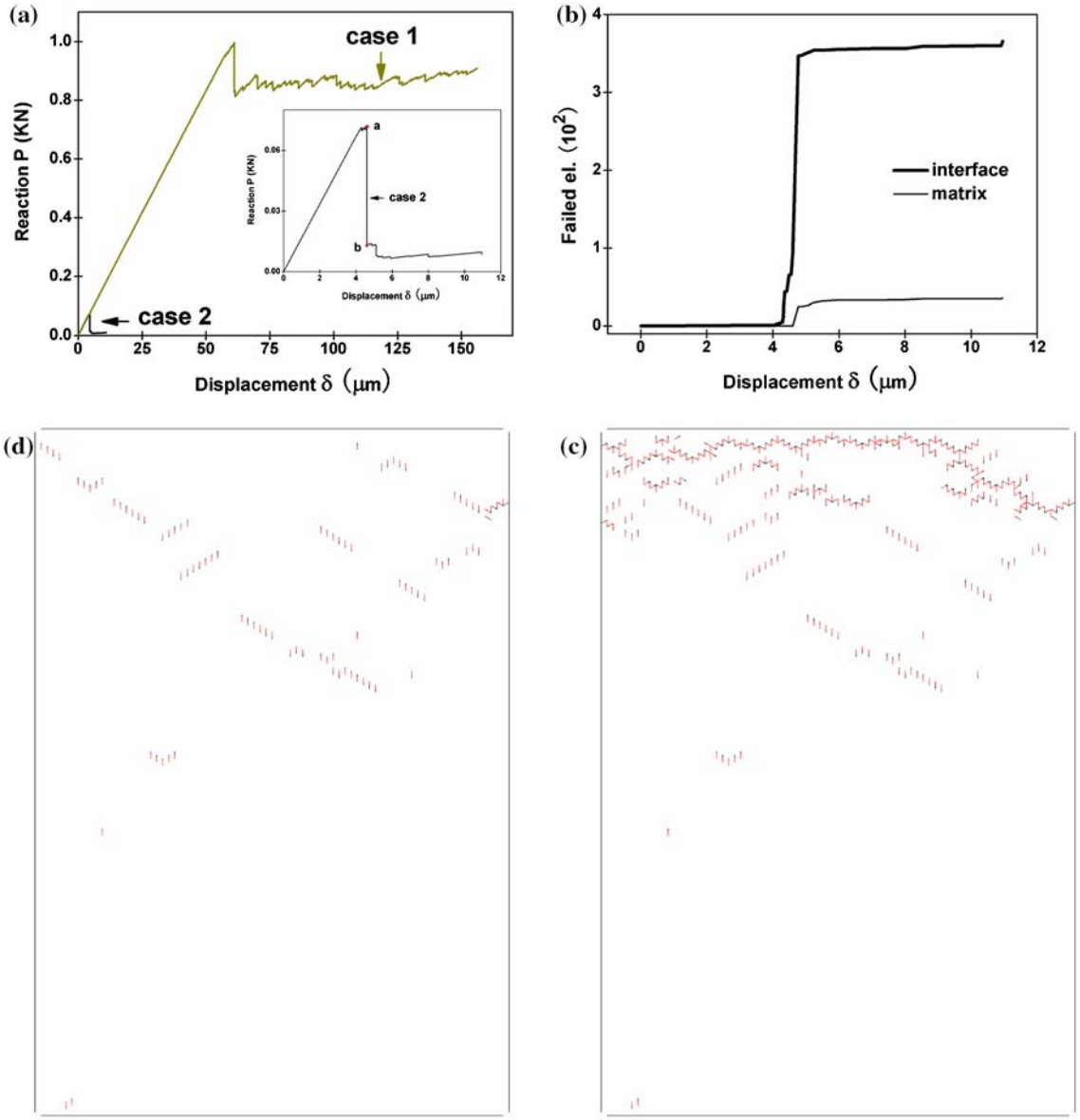

Fig. 9 In case 2, **a** the P-δ curve compared with case 1; **b** the cumulative number of cracked elements versus displacement; and distributions of cracked elements at two load levels: **c** for point a; **d** for point b

(3) In case 2, elements fail due to tension. In case 1, however, failure mechanisms include compression-induced tensile failure, compressive failure, and failure due to combined action of compression and shear, therefore the peak load of case 1 is the compositive indicator of the following three strengths: tensile strength, compressive strength and shear strength, instead of only compression strength.

Case 3: Influence of lateral confinement

The carrying capacity and crack patterns are strongly influenced by the nature and magnitude of confinement pressure [18]. In case 3, the lateral constraints along the left and right edges are regarded as lateral confinements. Figure 10a shows the confinement force versus controlled displacement, that is, the curve called "reaction on right edge".

The lateral constraint confines the horizontal dilatation of the specimen and leads to the following differences between case 3 and case 1:

(1) At the beginning of the curve, the slope of the pre-peak regime is larger than that in case 1 (Fig. 10a).

(2) The peak load is 1087.2N ($\delta = 61.0\mu$m), and is larger than that in case 1, 996.1N ($\delta = 61.1\mu$m). At the peak-load level, the total numbers of cracked elements are 109 for case 3 (Fig. 10b), and 925 for case 1 (Fig. 8b). It indicates that the specimen in case 1 is damaged much more seriously than the

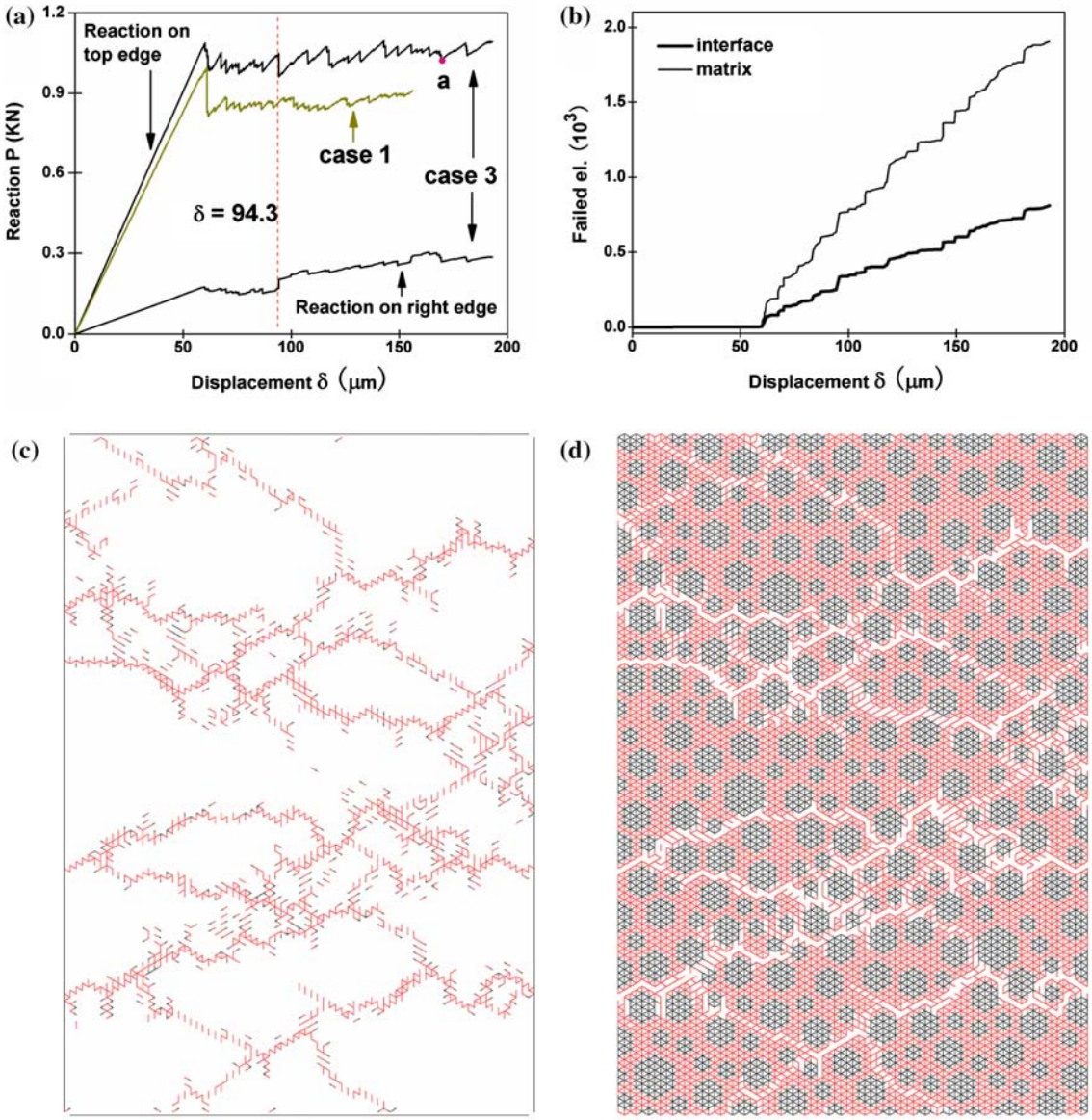

Fig. 10 In case 3, **a** the P-δ curve compared with case 1; **b** the cumulative number of cracked elements versus displacement; **c** distribution of cracked elements and **d** crack pattern at the load level a

specimen in case 3 at the peak load level, leading to the larger peak load in case 3. The confinement hampers the formation and growth of microscopic cracks during the pre-peak stage.

(3) The angle between the macroscopic cracks and the loading direction is much bigger than that in case 1. When the macro crack meets local compression-induced tensile cracks roughly parallel to the loading direction, its path is usually deflected and may extend along the loading direction temporarily. There are much more compression-induced tensile cracks in Case 1 (Fig. 8g, h) than case 3 (Fig. 10c, d), so the macro cracks in case 1 are influenced more frequently by tensile cracks than in case 3.

(4) At the end of the simulation, the percentage of fractured matrix elements is 69.6%, much larger than 38.9% in case 1. The reason is as follows: the vast majority of fractured interface elements consist of those due to compression-induced tensile actions, while the compression-induced tensile failures are more difficult to occur in case 3 than in case 1.

Additionally, the reaction on the loading platen and the reaction on the right edge vary differently with controlled displacement. For example, when $\delta = 94.3\mu$m (Fig. 10a), there occurs a steep drop in the former, but a steep increase happens in the latter. As more and more elements breaks, the material behaves more and more like a granular material.

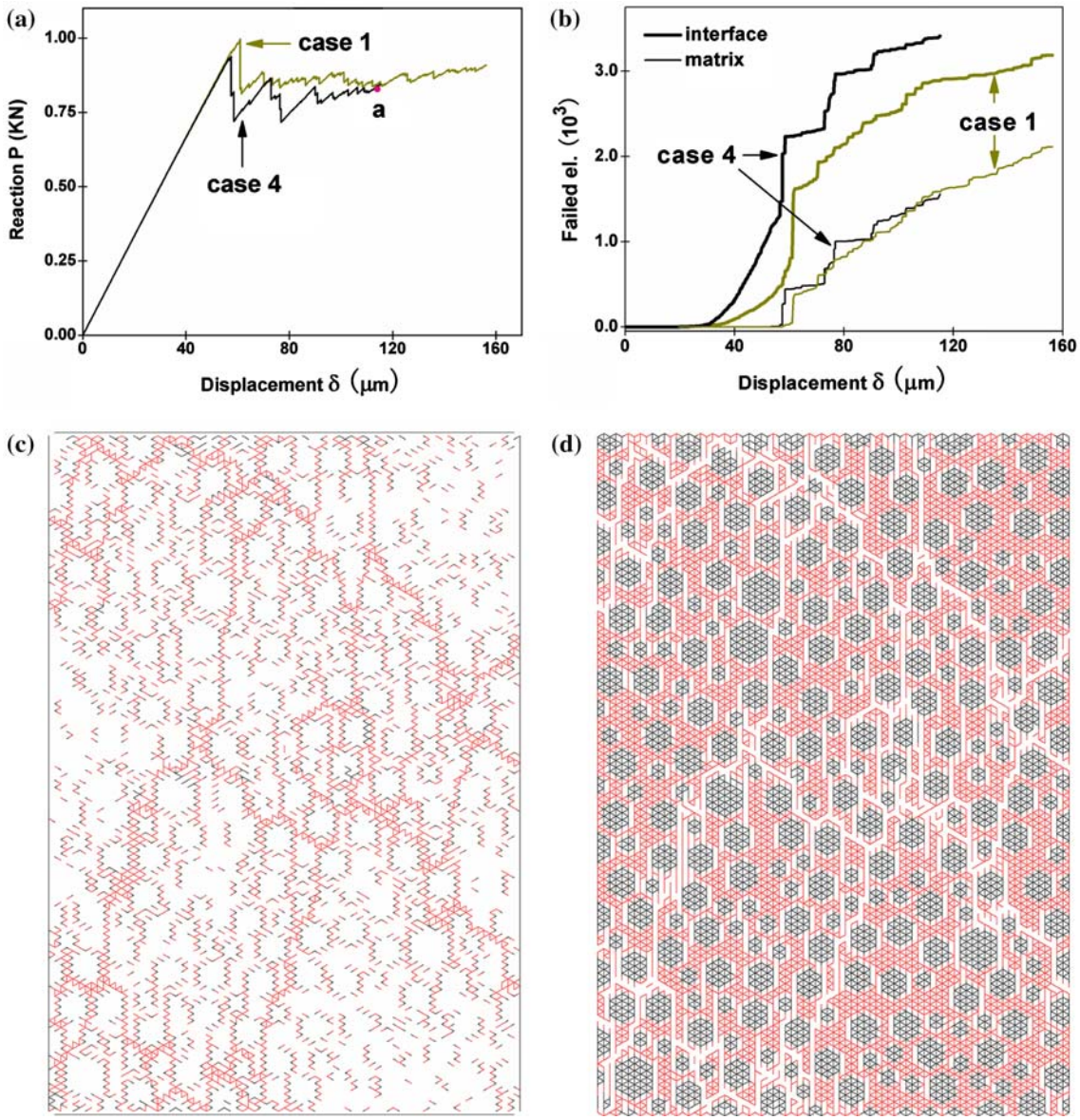

Fig. 11 In case 4, **a** the P-δ curve and **b** the cumulative number of cracked elements versus displacement compared with case 1; **c** distribution of cracked elements and **d** crack pattern at the load level a

Therefore, the lateral dilatation increases with the increase of failed elemental number, which is the reason for the steep increase of the lateral confinement reaction.

Case 4: Influence of friction angle

The unique different experimental condition between case 4 and case 1 is that case 4 has a smaller friction angle. It can be found from Fig. 5 that the safe domain in case 4 will be smaller than that in case 1. As a result, the specimen in case 4 will be destroyed more easily, or in other words has a lower carrying capacity. This is also shown in Fig. 11a, in which the peak load of case 4 is 937.8N, smaller than 996.1N in case 1.

The compressive strengths of the three material phases are the same as those in case 1 respectively, but the smaller friction angle makes failures by violating Eq. 13c happen less possibly than in case 1. In other words, elements parallel to loading direction will fail less possibly. As shown in Fig. 11b, the curve of the cumulative number of failed matrix number versus displacement is roughly the same as that in case 1, but the number of fractured interface elements is much larger than that in case 1 when the controlled displacement is fixed. By comparing Fig. 11c and d with Fig. 8g and h, it can be found that less failures of elements parallel to the loading direction happen than in case 1.

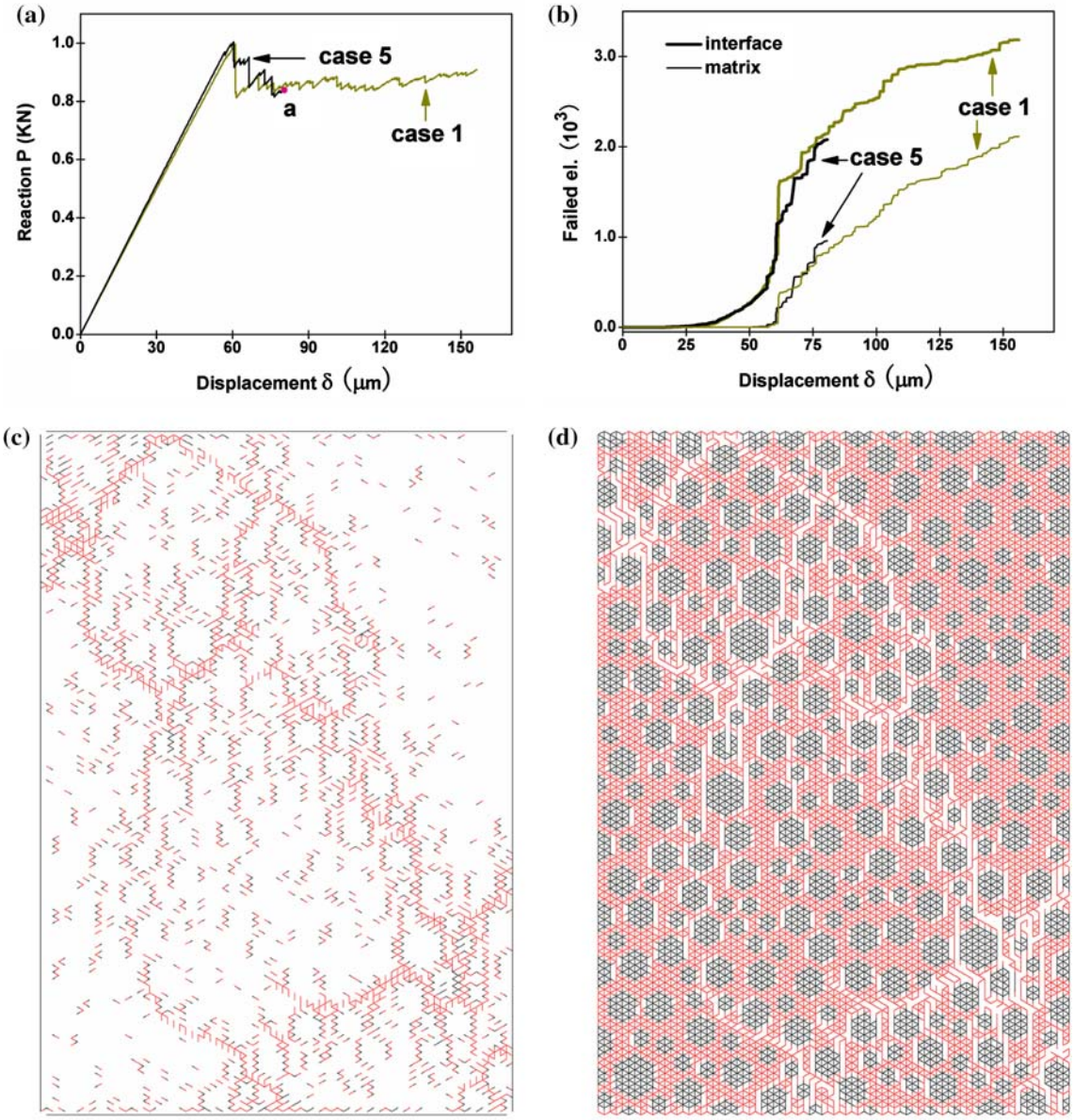

Fig. 12 In case 5, **a** the P-δ curve and **b** the cumulative number of cracked elements versus displacement compared with case 1; **c** distribution of cracked elements and **d** crack pattern at the load level a

Case 5: Influence of the loading-platen's stiffness

The stiffness of the loading platen influences the fracture behavior, especially the crack patterns [14,41]. The loading platen's stiffness in case 5 is five times of that in case 1. Stiffer loading platens confine the lateral dilatation near the platens: from Fig. 12c and d, it can be seen that the distribution of local cracks parallel to loading direction near two loading platens is much sparser than that in the middle of the specimen, and the parallel local cracks are generally longer than those near the loading platen. These phenomena are different from case 1.

The stiffer loading platen can be taken as a kind of lateral confinement from the viewpoint of hampering compression-induced tensile failures. Therefore, the peak load, the slope of the pre-peak stage in case 5 are both larger than those in case 1 (Fig. 12a), which is due to the reason similar to that in the confined case, that is, case 3. But, the difference between case 5 and case 1 (Fig. 12a) is much smaller than that between case 3 and case 1 (Fig. 10a), because the lateral confinement produced by the stiffer loading platen in case 5 is much weaker than that in case 3 where lateral displacements of both the right and left edges are set to zero.

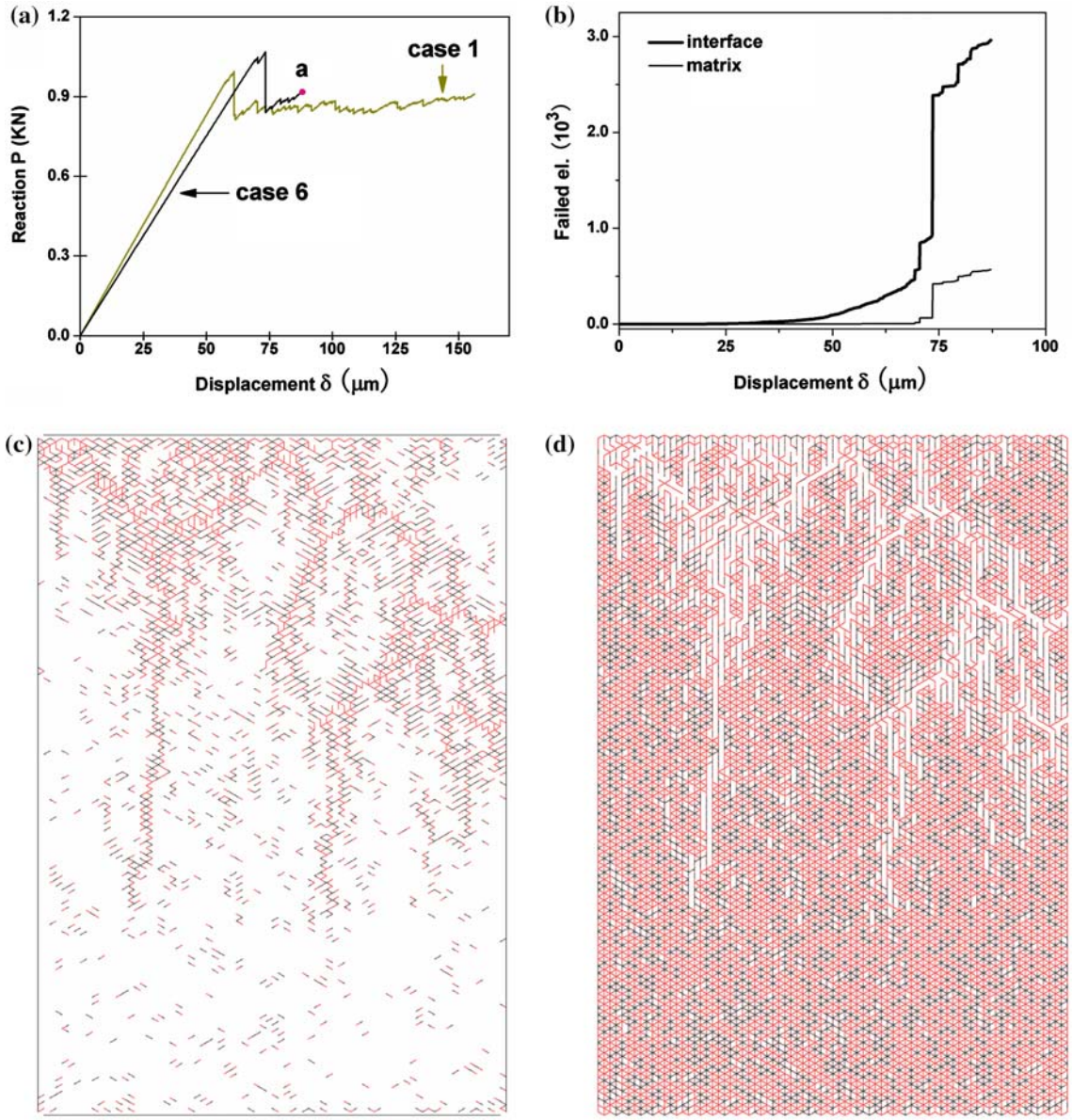

Fig. 13 In case 6, **a** the P-δ curve compared with case 1; **b** the cumulative number of cracked elements versus displacement; **c** distribution of cracked elements and **d** crack pattern at the load level a

The stiffer loading platen also makes the crack pattern in case 5 (Fig. 12c, d) obviously different from that in case 1 (Fig. 8g, h).

Case 6: Effectiveness of another kind of GB lattice

This case is conducted on the GB lattice proposed by [26], where every aggregate is modeled by a single node. The aim here is to show its effectiveness for simulating compressive failure.

The aggregate distribution, average radii of aggregates and aggregate volume content are all different from the other cases, so it is not necessary to compare them. The P-δ curve is also divided into the pre-peak stage and the post-peak stage by the peak load (Fig. 13a). The steep drop directly following the peak load corresponds to the steep increase of cracked elements (Fig. 13b). As shown in Fig. 13c and d, there are two macro cracks roughly parallel to the loading direction in the middle of the specimen, and several inclining macro cracks appear near the top edge. These features are all reasonable as discussed in case 1.

It is notable that the lattice having a total of 7,781 nodes accommodates 3,000 aggregates, but it can even accommodate more [26]. In consideration of its high accommodating capacity, this kind of GB lattice is preferred when the large problem is considered.

Case 7: Influence of aggregate inclusion

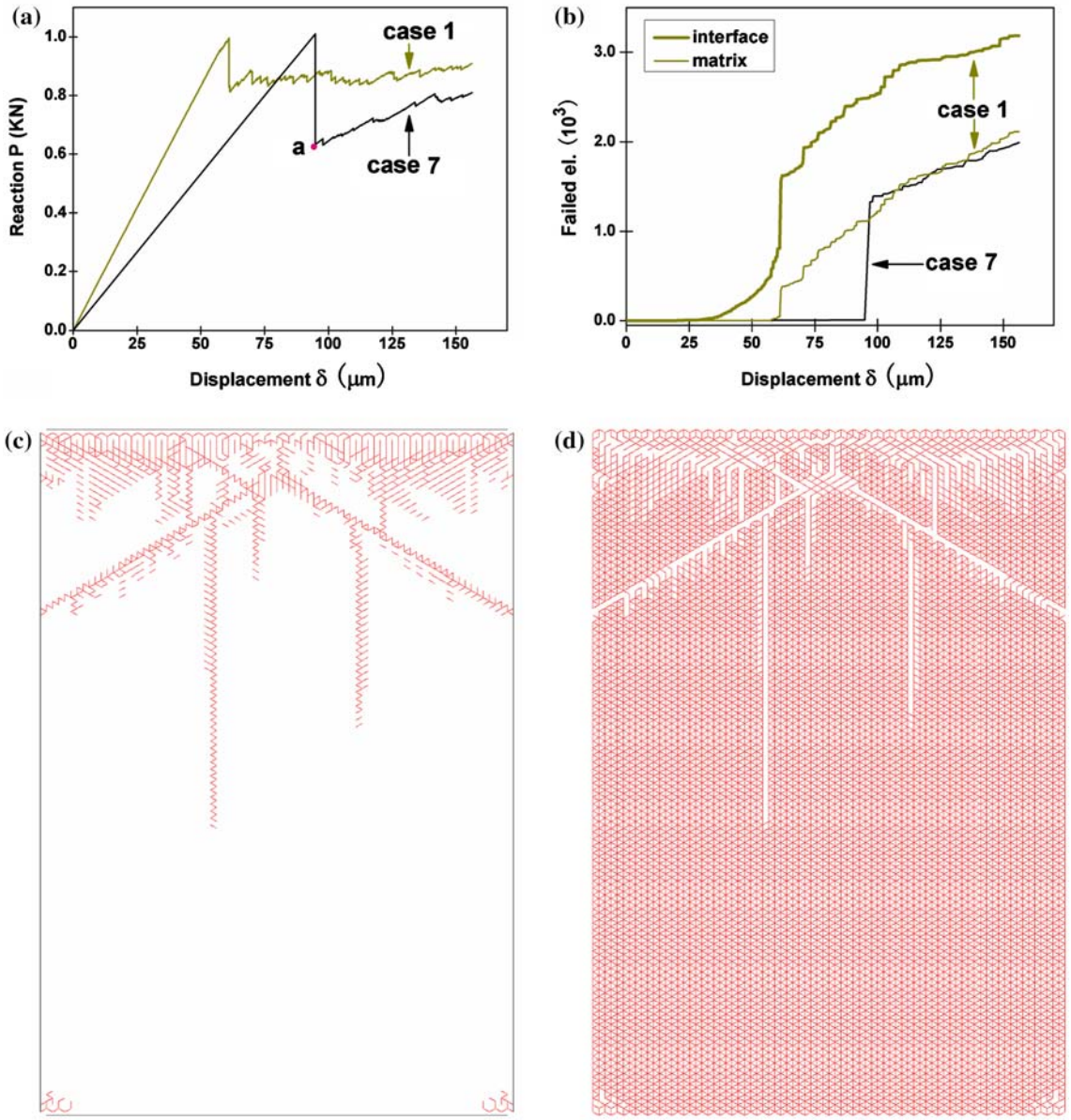

Fig. 14 In case 7, **a** the P-δ curve and **b** the cumulative number of cracked elements versus displacement compared with case 1; **c** distribution of cracked elements and **d** crack pattern at the load level a

In this case, the specimen is purely matrix-phased and has no inclusion of aggregates. Therefore, all kinds of toughening mechanisms due to particle structure, such as deflection and temporary blockage of crack extension, are excluded from this case. This leads to the following differences between case 7 and case 1:

(1) After the steep drop of load directly following the peak, load P becomes 62.6% of the peak load (Fig. 14a), much smaller than the corresponding percentage 83.0% in case 1, indicating that case 7 is much brittle than case 1, or equivalently less ductile than case 1 [25]. As shown in Fig. 14b, the number of cracked elements increases much steeply directly following the peak load than case 1.

(2) The slope of the pre-peak stage is much smaller than in case 1, indicating a lower capacity of bearing deformation. The inclusion of stiffer aggregates (Table 1) into matrix makes the specimen much stiffer that the purely matrix-phase specimen under the compressive condition. However, this feature disappears in the tensile condition [25,26,40] because aggregates are isolated by the surrounding interfaces and higher stress cannot be transferred onto aggregates, and the other reason is that the contact mechanism partly recurs the bearing capacity of many cracked elements in compressive tests.

(3) The crack pattern (Fig. 14c, d) is much more regular than that in case 1 (Fig. 8c, h). Case 7 roughly has two kinds of

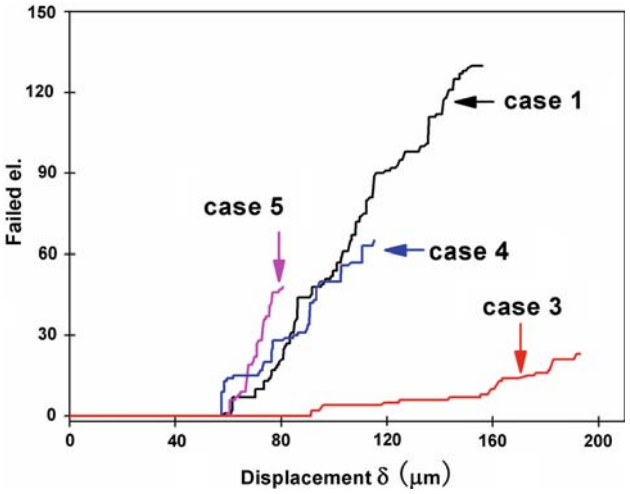

Fig. 15 The cumulative number of cracked aggregate elements versus displacement compared for case 1, case 3, case 4 and case 5. Note that there is no aggregate failed in case 2, case 6 and case 7

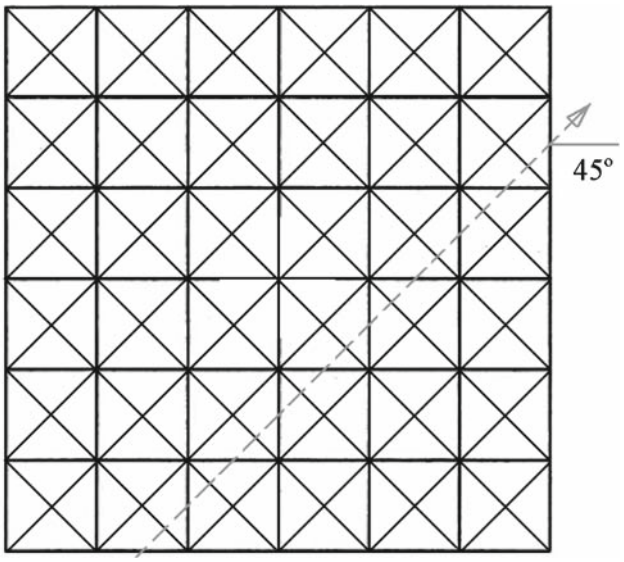

Fig. 16 A lattice apt to fail along ±45°

macro cracks: two shear deformation crack bands near the top edge and forming an angle of 30° with the horizontal loading platens, and several straight splitting cracks around the shear bands. At the middle and bottom domain of the specimen, there are seldom distributed micro failures. However, case 1 shows the completely different feature: macro cracks become extremely irregular due to the inclusion of aggregates and a large amount of local cracks form around aggregates because stress concentrations happen under external loads.

Then the direction of shear deformation crack bands is discussed. In case 7, two shear deformation crack bands form an angle of 120° with each other. Similar phenomena have been discussed in literature. For example, Gao and Klein [15] simulated the crystalline material by using the virtual internal bond (VIB) model which is a kind of regular triangular lattice in nature [10,11], and showed highly localized shear deformation bands emanating at roughly ±60° to the original direction of crack propagation. This kind of localized shear deformation does not represent the action of plasticity since the employed VIB materials are all purely elastic, but the results do highlight the effects of deformation induced elastic anisotropy.

Our explanation for the regular direction ±60° of shear deformation crack bands in this homogeneous case is the adoption of regular triangular lattice. The first author, Liu, who investigated the truss lattice model several years ago, finds that lattices of different geometries produce different directions of shear deformation bands. For triangular lattice, the direction is around ±60°; for the lattice shown in Fig. 16; however, the direction becomes ±45°.

However, this kind of cracking directional dependency on the geometry of lattices will not influence the effectiveness of GB lattice for simulating heterogeneous media such as concrete. Concrete is highly heterogeneous due to inclusion of aggregates and is never the homogeneous material such as crystalline. The path of cracks depends almost completely on randomly distributed aggregates and initial micro fractures throughout concrete. The particle structure will deflect the crack direction or hamper the extension of cracks temporarily, leading to extremely irregular paths of macro cracks, which can be found from the crack patterns of all above six heterogeneous cases, that is, case 1–6.

5 Conclusions

To extend the practical application of the GB lattice model, a novel algorithm for simulating compressive failures was proposed by adopting the Mohr–Coulomb strength criterion and the event-by-event detecting technique. Furthermore, this algorithm was implemented in a finite element code. The possible events considered here can be the compression-induced tensile failure, the failure due to combined action of shear and normal stress, the failure due to compression, contact/separation of crack surfaces. The smooth-contact assumption was adopted, but it is not a too rough approximation because numerical tests showed that the interlocking is the dominant toughening mechanism and hampers the extension of shear deformation crack bands frequently.

Numerical tests were conducted on a concrete plate subjected to compression. Results of the uniaxial compression case were compared with those of uniaxial tension. Furthermore, influences of lateral confinement, friction angle, stiffness of loading platen, inclusion of aggregates on failure behaviors were respectively analyzed in detail.

In the case study, specimens with exactly the same micro structure as well as macro sizes were employed. Due to this reason, the influence of micro structures can be excluded when analyses of some special influence factor such as the friction angle or lateral confinements are conducted. This kind of case study can hardly be implemented completely in physical experiments. Even though physical experimental techniques are adequately satisfactory, it is almost impossible to produce two specimens of the same micro structure. As a result, the comparative analyses like those in this paper are hampered by the considerable influence of micro structures, especially for heterogeneous media such as concrete and rock. This is a common advantage of all numerical models.

Acknowledgments This research work was sponsored by National Natural Science Foundation of China through Grant No. 10572140, No. 10232050 and No. 10721202. The first author, Jinxing Liu, is greatly grateful to Dr. Xuejun Wang for his valuable discussions on the Mohr-Coulomb criterion, and to Dr. Xiaojiang Shang for his valuable discussions on general knowledge about concrete's nonlinear behavior.

References

1. Bazant ZP, Tabbara MR, Kazemi MT, Cabot GR (1990) Random particle model for fracture of aggregate or fiber composites. J Eng Mech 116(8):1686–1705
2. Bolander JE Jr, Shiraishi T, Isogawa Y (1996) An adaptive procedure for fracture simulation in extensive lattice networks. Eng Fract Mech 54(3):325–334
3. Bolander JE Jr, Saito S (1998) Fracture analysis using spring network with random geometry. Eng Fract Mech 61(5–6):569–591
4. Chang CS, Gao J (1996) Kinematics and static hypothesis for constitutive modeling of granulates considering particle rotations. Acta Mech 115:213–229
5. Chang CS, Wang TK, Sluys LJ, van Mier JGM (2002) Fracture modeling using a micro-structural mechanics approach—I. Theory and formulation. Eng Fract Mech 69:1941–1958
6. Chang QT (1994) Nonlinear dynamic discontinuous deformation analysis with finite element meshed block systems. PhD Thesis, University of California, Berkeley
7. Chetouane B, Dubois F, Vinches M, Bohatier C (2005) NSCD discrete element method for modeling masonry structures. Int J Numer Meth Eng 64(1):65–94
8. Cundall PA, Strack ODL (1979) A discrete numerical model for granular assemblies. Geotechnique 29(1):47–65
9. Cusatis G, Bazant ZPF, Cedolin LM (2003) Confinement-shear lattice model for conrete damage in tension and compression: I. Theory J Eng Mech 129(12):1439–1448
10. Deng SC, Liu JX, Zhang J, Liang NG (2006) Component assembly model and its application to quasi-brittle damage. Theor Appl Fract Mech 46:232–242
11. Deng SC, Liu JX, Zhang J, Liang NG (2007) Validation of component assembly model and its extension to plasticity. Theor Appl Fract Mech 47:244–259
12. Diebels S, Steeb H (2002) The size effect in foams and its theoretical and numerical investigation. Proc R Soc Lond A 58:2869–2883
13. Digby PJ (1981) The effective elastic modulli of porous granular rock. ASME J Appl Mech 48:803–808
14. Ferro G (2006) On dissipated energy density in compression for concrete. Eng Fract Mech 73:1510–1530
15. Gao HJ, Klein P (1998) Numerical simulation of crack growth in an isotropic solid with randomized internal cohesive bonds. J Mech Phys Solids 46(2):187–218
16. Goodman RE, Shi G (1985) Block theory and its application to rock engineering. Prentice-Hall, Englewood Cliffs
17. Herrmann HJ, Roux S (1992) Statistical models for the fracture of disordered media. Elsevier, Amsterdam
18. Huang CY, Subhash G (2003) Influence of lateral confinement on dynamic damage evolution during uniaxial compressive response of brittle solids. J Mech Phys Solids 51:1089–1105
19. Hughes TJR, Taylor RL, Kanoknukulchai S (1977) A simple and efficient finite element for bending. Int J Numer Eng 11: 1529–1543
20. Ibrahimbegovic A, Depaplace A (2003) Microscale and mesoscale discrete models for dynamic fracture of structures built of brittle material. Comput Struct 81:1255–1265
21. Karihaloo BL, Shao PF, Xiao QZ (2003) Lattice modelling of the failure of particle composites. Eng Fract Mech 70:2385–2406
22. Kawai T (1978) New discrete models and their application to seismic response analysis of structures. Nucl Eng Des 48:207–229
23. Krajcinovic D (2000) Damage mechanics: accomplishments, trends and needs. Int J Solids Struct 37:267–277
24. Lemaitre J (1996) A course on damage mechanics (in Chinese). Science Press, Beijing
25. Lilliu G, van Mier JGM (2003) 3D lattice type fracture model for concrete. Eng Fract Mech 70:927–941
26. Liu JX, Deng SC, Zhang J, Liang NG (2007) Lattice type of fracture model for concrete. Theor Appl Fract Mech 48:269–284
27. Liu JX, Deng SC, Liang NG (2008) Comparison of the quasi-static method and the dynamic method for simulating fracture processes in concrete. Comput Mech 41:647–660
28. Liu JX, Deng SC, Zhang J, Liang NG (2007) Beam lattice modeling for the fracture of particle composites. Eng Mech (accepted)
29. Ostoja-Starzewski M (2002) Lattice models in micromechanics. Appl Mech Rev 55:35–60
30. Ostoja-Starzewski M (2007) Microstructural Randomness and scaling in mechanics of materials. Chapman & Hall/CRC, Boca Raton
31. Potyondy DO, Cundall PA (2004) A bonded-particle model for rock. Int J Rock Mech Min Sci 41:1329–1364
32. Prado EP, van Mier JGM (2003) Effect of particle structure on mode I fracture process in concrete. Eng Fract Mech 70: 1793–1807
33. Rots JG, Belletti B, Invernizzi S (2007) Robust modeling of RC structures with an "event-by-event" strategy. Eng Fract Mech (in press)
34. Schlangen E, van Mier JGM (1992) Experimental and numerical analysis of the micromechanics of fracture of cement-based composites. Cem Conc Comp 14(2):105–118
35. Schlangen E, Garboczi EJ (1997) Fracture simulation of concrete using lattice models: computational aspects. Eng Fract Mech 57(2–3):319–332
36. Schorn H, Rode U (1987) 3-D modeling of process zone in concrete by numerical simulation. In: Shah SP, Swartz SE (eds) Fracture of concrete and rock. Springer, New York pp 220–228
37. Shi G (1988) Discontinuous deformation analysis—a new numerical model for the statics, dynamics of block systems. PhD Thesis, University of California, Berkeley
38. Shyu K (1993) Nodal-based discontinuous deformation analysis. PhD Thesis, University of California, Berkeley
39. Trovalusci P, Masiani R (2003) Non-linear micropolar and classical continua for anisotropic discontinuous materials. Int J solids struct 40:1281–1297

40. van Mier JGM, van Vliet MRA, Wang TK (2002) Fracture mechanisms in particle composites: statistical aspects in lattice type analysis. Mech Mater 34:705–724
41. van Vliet M, van Mier JGM (1995) Softening behaviour of concrete under uniaxial compression. In: Wittmann F (ed) Fracture mechanics of concrete structures. AEDIFICATIO Publishers, Freiburg, pp 383–396
42. Walton K (1987) The effective elastic modulli of a random packing of spheres. J Mech Phys Solids 35:213–226
43. Wang TK, van Mier JGM, Bittencourt TN (2001) Statistical study of fracture in concrete. In: Ravi-Chandar K, Karihaloo BL, Kishi T, Ritchie RO, Yokobori AT Jr, Yokobori T (eds) Advances in fracture research, Proc ICF10 0665OR. Pergamon, New York
44. Wang XC (2003) Finite element method, 1st edn. Tsinghua University Press, Beijing